

# 1 Palaeotidal atlas of the UK for the last 2 10,000 years

3 Jon Hill<sup>1</sup>

4 <sup>1</sup>Department of Environment and Geography, University of York.

## 5 ABSTRACT

6 Over the past 10,000 years the UK has seen dramatic changes to its coastline due to sea-level  
7 rise. Past changes in sea level can be estimated from analysis of sedimentary deposits,  
8 including any microfossil assemblages found within. Once dated and the elevation is known,  
9 these data become sea level index points (SLIPs). In recreating past sea level in this way there  
10 is an implicit assumption of no change to the tidal regime, despite the fact we know this not to  
11 be true. Here, I present modelling simulations of the tides of the UK for the past 10,000 years  
12 based on current estimates of palaeoshorelines and bathymetry. I validate the tidal model on  
13 modern tidal gauges using the 0 m contour as a shoreline as well as modern shoreline data,  
14 before using the same model to create 30 day tidal simulations at 1,000 year intervals. This  
15 palaeotidal atlas can be used to estimate both maximum tidal heights and tidal range which in  
16 turn could be used to correct SLIPs. The results are consistent with previous estimates, despite  
17 differences in estimated palaeobathymetry, boundary conditions and numerical technology  
18 used. The tidal maps published will have a wide range of uses across Quaternary science.

19 Keywords: sea level, modelling, tides

## 20 INTRODUCTION

21 During the Holocene the Northwest European continental shelf sea has been transformed due  
22 to sea-level rise due to deglaciation of the Fennoscandian ice sheet. Eustatic sea level has  
23 risen some 130 m meters over the last 16,000 years with the majority of that change taking place  
24 between 16,000 and 7,000 years (Lambeck et al., 2014). Not only does the rise vary temporally,  
25 but due to isostatic rebound, relative sea level also varies spatially. This legacy is still relevant  
26 today as the UK is experiencing differential rates of relative sea level rise with the south of the  
27 UK experience much higher rates of relative sea level rise than the north (Shennan et al., 2018).

28 In order to assess past sea-level changes we need to find evidence of where the sea level  
29 was in the past. This evidence can be geomorphological (e.g. raised beaches), palaeontological  
30 or sedimentological (e.g. marine sediments), archaeological (Shennan, 2015). By dating these  
31 data, along with accurate measurements of location, the direction sea level is moving in and  
32 height above/below modern mean water height (Shennan, 2015), the data can be termed a Sea  
33 Level Index Point (SLIP). However, most SLIPs are data within the tidal range; that is they  
34 represent some measure of water level, but not necessarily the mean sea level (Hill, 2016; van de  
35 Plassche, 1986). Therefore, to interpret the SLIP as mean sea level a tidal range is required.  
36 Without any other information available, modern tidal ranges are used.

37 Previous numerical modelling studies have already established that tidal range can change  
38 dramatically with changing sea levels. Previous studies have tended to focus on a smaller area,  
39 e.g. the Wash or have used relatively coarse resolution of several km over the NW European shelf.  
40 One of the first such models that used more than a simple M<sub>2</sub> forcing was that of Hinton (1992)  
41 which modelled the southern North Sea coast of England using a 3 km regular grid. Hinton

42 reconstructed palaeobathymetry simply by reducing or increasing sea level uniformly across the  
43 grid. Similar methods were employed by [Austin \(1991\)](#), who also examined the changes in tidal  
44 dissipation and tidal fronts. Models have since been developed that made use of GIA models,  
45 such as those of [Shennan and Horton \(2002\)](#) and [Neill et al. \(2010\)](#). The inclusion of a GIA  
46 model to estimate palaeobathymetric changes take into account the spatial nature of the changes.  
47 The most recent NW shelf model was that of [Ward et al. \(2016\)](#) which used a relatively coarse  
48 computational mesh of around 4.5 km (1/24 of a degree) and looked at changes to bed shear  
49 stress as well as tidal dynamics. All previous models show substantial changes in the Mean High  
50 Water Spring Tides and tidal range due to sea-level changes in the UK.

51 The result of palaeotidal models can be used to correct SLIPs for palaeo-tidal range. [Neill  
52 et al. \(2010\)](#) suggested this to be the case, but noted the inherent circularity of the problem –  
53 correcting SLIPs alters the GIA model, which in turn alters the palaeobathymetry and then the  
54 tidal range estimates. [Neill et al. \(2010\)](#) suggest a procedure whereby some SLIPs are held  
55 back from the GIA model used to define the palaeobathymetry of the tidal model to provide a  
56 verification-calibration study. [Ward et al. \(2016\)](#) agree that this methodology could be useful  
57 and also that higher resolution models are better suited to this as SLIPs are often found near  
58 coastlines or in estuaries.

59 Here, I use multiscale modelling on an unstructured mesh with resolution varying from  
60 20 km to 1.5 km around the coastlines, with palaeobathymetry derived from the 2011 GIA  
61 modelling of [Bradley et al. \(2011\)](#). This is the first time a multiscale approach has been used in  
62 this way and that all model outputs made freely available for further study. Unstructured mesh  
63 models have particular advantages when modelling complex coastlines and bathymetries as they  
64 avoid the ‘staircase effect’ ([Wells et al., 2005a](#)) typically seen in structured mesh models (Fig. 1).  
65 Increasing resolution to where it is needed (e.g. coastlines or rapid changes in bathymetry) means  
66 that the accuracy of a higher resolution model is obtained whilst minimising computational  
67 expense.

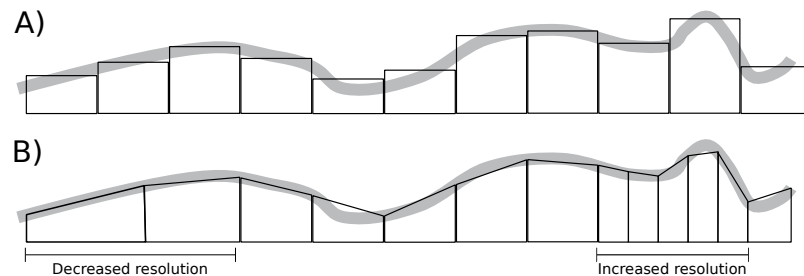


**Figure 1.** Example of the ‘staircase effect’ when modelling bathymetry. The thick grey line is the actual bathymetry. In the structured grid model (A) this is represented as a value in a cell, resulting in sharp edges where bathymetry changes more quickly than the mesh size can resolve. In contrast an unstructured grid model can use linear functions within cells (or indeed higher order functions) and change resolution where needed. Unstructured mesh models typically take longer to solve for the same resolution, however.

68 In this paper, I outline the details of the model set-up used before validating this model on  
69 the modern UK tidal gauge data. I then detail the set up for the palaeotidal models and then  
70 present results of the tidal atlas at 1,000 year intervals. Results are shown for a number output  
71 parameters including tidal stratification estimates. I conclude by discussing the implications  
72 of this study in terms of correcting the European SLIP database and how we could avoid the  
73 circularity problem.

## 74 METHODS AND MATERIALS

75 The palaeotides were calculated using the Fluidity model, which is a highly flexible finite  
76 element/control volume modelling framework which allows for the numerical solution of a  
77 number of equation sets (Piggott et al., 2008) and has been used in a variety of tidal studies,  
78 including both modern and ancient tides on regional and global scales (Wells et al., 2005b,a,  
79 2007, 2010; Martin-Short et al., 2015; Collins et al., 2017, 2018). One of the major advantages  
80 of Fluidity is the use of a multiscale mesh, which can resolve fine-scale details even in a regional  
81 setting using resolution down to metre-scale (Martin-Short et al., 2015).

### 82 Fluidity

Here, the depth-averaged shallow water equations are solved in a rotating reference frame in non-conservative form:

$$\begin{aligned} \frac{\partial u}{\partial t} + u \cdot \nabla u + fu^T - \nabla v \left[ \nabla u + (\nabla u)^T \right] + g \nabla \eta &= -c_b \frac{\|u\|u}{H}, \\ \frac{\partial \eta}{\partial t} + \nabla \cdot (Hu) &= 0, \end{aligned} \quad (1)$$

83 where  $u$  is the 2D, depth-averaged velocity vector,  $t$  represents time,  $\eta$  is the free surface  
84 perturbation,  $H$  is the total water depth, and  $v$  is the kinematic viscosity. The Coriolis term,  
85  $fu^T$ , consists of  $u^T$ , the velocity vector rotated counter-clockwise over  $90^\circ$ , and  $f = 2\Omega \sin(\zeta)$ ,  
86 with  $\Omega$  the angular frequency of Earth's rotation and  $\zeta$  the latitude. The dimensionless friction  
87 coefficient  $c_b$  represent respectively the background bottom drag (assumed constant here).

88 The equations (1) are discretised on a mixed finite element pair, with a continuous Galerkin,  
89 piecewise quadratic formulation for the free surface (P2) and a piecewise linear discontinuous  
90 Galerkin approximation (P1<sub>DG</sub>) for velocity. The resulting P1<sub>DG</sub>P2 velocity/free-surface dis-  
91 cretisation has a number of desirable properties described fully in Cotter et al. (2009a,b); Cotter  
92 and Ham (2011). In addition to the discretisation of the linear shallow water terms described  
93 therein, we employ a standard P1<sub>DG</sub>-discretisation with upwind fluxes and slope limiting for the  
94 advection term and the Compact Discontinuous Galerkin scheme Peraire and Persson (2008), for  
95 the viscosity term.

96 A two-level  $\theta$  method is employed for time-integration, combined with explicit subcycling  
97 for the advection step. Here  $\theta = 0.53$ , which is close to the Crank-Nicolson scheme, and  
98 therefore minimises wave dissipation whilst maintaining stability. Two Picard iterations per  
99 time-step are used to linearise the nonlinearity in the advection and friction terms. Finally, the  
100 linear discretised systems are solved using iterative sparse linear solvers available in PETSc  
101 Balay et al. (2018). More details on the spatial and temporal discretisations available in Fluidity  
102 are described in Imperial College London AMCG (2015) and Piggott et al. (2008).

### 103 Model setup

104 The model domain consisted of the entire NW European continental shelf, bordered by coastlines  
105 and the Danish Straits (Fig. 2). For present day simulations two coastlines types were modelled.  
106 One using the high resolution GSHHS coastline dataset (Wessel and Smith, 1996), the other  
107 using the 0 m contour. For each timeslice from 1 ka to 10 ka, modern bathymetry derived from  
108 GEBCO 2014 (Weatherall et al., 2015) was adjusted according to the glacio-isostatic adjustment  
109 (GIA) model of Bradley et al. (2011) to create a palaeobathymetry. For each palaeobathymetry,  
110 a coastline derived from the 0 m contour was created, which served as a numerical boundary.  
111 This was trimmed to meet the western boundary and the boundary at the Denmark Straits. The  
112 mesh resolution varied with highest resolution along coastlines (1.5 km triangles), 3 km along  
113 other boundaries and 25 km between 50 and 100 km away from a boundary. In addition, a mesh

114 metric based on idealised wave celerity increased resolution in deeper water where the tidal wave  
 115 moves quickest (Lambrechts et al., 2008) via:

$$50000.0 * \sqrt{\frac{10.0}{h}} \quad (2)$$

116 where  $h$  is the water depth. All points on the coastlines and boundaries were joined using a  
 117 B-spline curve to produce a smooth boundary for the final mesh. All meshes were constructed in  
 118 (qmesh) (Avdís et al., 2018).

119 The coastlines and sea bed were set to no-normal flow with a Manning quadratic drag  
 120 formulation applied with a drag coefficient of 0.025. The open boundary was forced via free  
 121 surface using the FES2014 data (Lyard et al., 2006). A short boundary section between coastline  
 122 and the open boundary was set to a no-slip boundary. Bathymetry was ‘dredged’ to ensure the  
 123 minimum water depth was 6 m to prevent stability issues as the model does not include wetting  
 124 and drying. Each model was spun up for 30 days, before then being run for another 30 days. The  
 125 final 30 days were used for all subsequent analyses.

### 126 **Modern validation**

127 To assess model performance I compared the model against tide gauge data from around the UK  
 128 using the two different methods of coastlines generation for the present day (0 m contour and  
 129 GSHHS). The two modern models were forced along the boundary of the continental shelf using  
 130 FES 2014 data and eight principle tidal components,  $M_2$ ,  $S_2$ ,  $N_2$ ,  $K_2$ ,  $O_1$ ,  $Q_1$ ,  $K_1$ , and  $P_1$ . The  
 131 constituents  $M_2$  and  $S_2$  are the dominant components on the NW European continental shelf.  
 132 The model was run for a total of 60 days, with the first 30 days considered as ‘spin-up’. Free  
 133 surface height data were then analysed at each tidal gauge location to produce model estimates  
 134 of  $M_2$ ,  $S_2$ ,  $K_1$ , and  $O_1$  amplitude and phases and compared to the data from tide gauges. To  
 135 compare the model against the tide gauges we use the method of Cummins and Thupaki (2017),  
 136 whereby error,  $\xi$  is calculated over the  $L$  tidal gauges as:

$$\xi = L^{-1} \sum D_L \quad (3)$$

$$D_L = \left[ \frac{1}{2} (A_o^2 + A_m^2) - A_o A_m \cos(\phi_o - \phi_m) \right]^{\frac{1}{2}} \quad (4)$$

137 where  $A_m$  is the modelled amplitude,  $A_o$  is the observed amplitude,  $\phi_o$  is the observed phase and  
 138  $\phi_m$  is the modelled phase, at each tidal gauge location. A separate  $D$  is calculated for each tidal  
 139 constituent modelled.

140 In the modern day, the mode has an error of 0.27 - 0.39 cm for  $M_2$  and 0.06 - 0.03 cm for  
 141  $S_2$  across 40 or 41 tidal stations (0 m contour or GSHHS coastline respectively), corresponding  
 142 to a 0.14 - 0.22 and 0.06 - 0.09 % error respectively according to equation 4. Fluidity appears  
 143 to slightly under predict the  $O_1$  component and over predict the  $K_1$  component compared to  
 144 tide gauges at higher amplitudes, but the mean semi-diurnal components show an excellent  
 145 agreement (Fig. 3). Both GSHHS and 0 m contour derived coastlines perform well overall.

146 The spatial distribution of the  $M_2$  tide and tidal range matches previous modelling studies  
 147 (Fig. 4). A major control on sediment movement in the NW European shelf sea are tidal currents  
 148 (Fig 4). Ward et al. (2015) developed a proxy for tidally induced bed shear stress and sediment  
 149 grain size which attempts to account for additional controls on sediment movement such as  
 150 waves and storm events. Here, I use this proxy across the whole NW continental shelf to derive  
 151 grain size estimates from tidal bed shear stress. The modelling results (Fig. 4) show the North

Model	M <sub>2</sub> error	S <sub>2</sub> error	K <sub>1</sub> error	O <sub>1</sub> error	No. Stations
GSHHS (%)	0.22%	0.06%	0.07%	0.08%	41
GSHHS (cm)	0.39	0.03	0.07	0.08	41
0m (%)	0.14%	0.09%	0.82%	0.87%	40
0m (cm)	0.27	0.06	0.08	0.08	40

152 Sea grain size as generally coarse sand, fining to very fine sand or less towards Norway. The  
153 Celtic Sea is dominated by medium to coarse sand grains, with a ribbon of very coarse sand  
154 running south from Scotland, through the Isle of Mann towards the Irish coast, before turning  
155 more easterly towards Wales. Similarly, the Severn Estuary is also coarse sand. The English  
156 channel is also dominated by coarse sands with some Gravel patches on the French coast. The  
157 coarse sediment is discontinuous in the easterly direction with patches of medium sand. The  
158 results in the Celtic Sea are entirely consistent with [Ward et al. \(2015\)](#) as well as observations by  
159 [Bockelmann et al. \(2018\)](#).

## 160 PALAEO-TIDAL CHANGES

161 The M<sub>2</sub> tidal component is the dominant component over most of the of NW European continental  
162 shelf. At 10 ka, an amphidromic point is situated near the palaeo-coastline in the North Sea  
163 (Fig. 5). There is a further point further north near Norway. At this time there is a significant  
164 reduction in M<sub>2</sub> amplitude across the whole seaway. When the land bridge between the UK and  
165 mainland Europe forms around 9 ka, these points become separated by the land bridge with  
166 a single amphidromic point in the English channel and two to the north and south of Dogger  
167 Bank respectively. The shallowing of the Dogger Bank area in the southern North Sea creates  
168 additional amphidromic points in the area which then precipitates a reduction in M<sub>2</sub> amplitude  
169 in the English Channel. By the time Dogger Bank becomes emergent at around 8 ka, there are  
170 complex tidal dynamics in the southern area of the North Sea, with four amphidromic points  
171 occurring in the area. At 7 ka the amphidromic points shift towards the modern configuration,  
172 with an additional point off the palaeo-coast of Denmark. Between 6 and 0 ka there is no major  
173 shift in the amphidromic points and moderate changes in M<sub>2</sub> tidal amplitude. There is, however,  
174 a minor shift at 4ka. The amphidromic point shifts towards the UK coast from the east of the  
175 North Sea at this time. This then reduces the M<sub>2</sub> amplitude slightly on the eastern coast of  
176 the UK. The driver for this appears to be sea-level change on the north coast of Europe. In  
177 the modern, the Severn Estuary and Brittany coast experience high tidal ranges due to the M<sub>2</sub>  
178 component. The modern North Sea shows amphidromic points (points where phase contours  
179 converge) near the Danish coast and in the northern part of the English Channel.

180 Comparing to previous studies ([Neill et al., 2010](#)) and ([Ward et al., 2016](#)), the estimates  
181 presented here show very similar spatial features as well as absolute values of M<sub>2</sub> tidal amplitude  
182 and phase. There are minor variations in the location of amphidromic points. The models results  
183 here show an additional amphidromal points off the coast of Norway at 10 ka compared to the  
184 results of [Neill et al. \(2010\)](#) and ([Ward et al., 2016](#)). There is very little difference in the M<sub>2</sub>  
185 amplitudes, however. At 8 ka all models show a complex set of amphidromic points in the  
186 southern North Sea, with similar patterns of M<sub>2</sub> amplitude.

187 These changes in the M<sub>2</sub> tide causes shifts in tidal range over the time period studies (Fig.  
188 6). The tidal range at 10 ka is much lower than modern day due to the much lower sea level.  
189 At 9 ka there is also an increase in tidal range in the Celtic Sea and the Severn Estuary closer  
190 to modern values. When the English Channel opens at 8 ka the tidal range is consistent with  
191 modern day. The tidal range stays generally consistent to the modern day ranges, apart from  
192 a minor change around 4 ka due to the changes in M<sub>2</sub> described above. These results mirror

193 those of Neill et al. (2010), which show a rapid reduction of tidal range between 0 and 10 ka  
194 with most of that change taking place at some point between 6 ka and 10 ka. However, the tidal  
195 range estimates presented here at 10 ka are slightly lower than that of Neill et al. (2010).

### 196 **Tidal mixing**

197 Tidal mixing occurs when the tidal currents are strong enough to induce turbulence via shear on  
198 the sea bed. There is therefore a relationship between water depth, tidal velocity and mixing in  
199 the water column which can be described using the Hunter-Simpson parameter,  $H_s$ ,

$$H_s = \log_{10} \frac{h}{u^3} \quad (5)$$

200 where  $h$  is the water depth (m) and  $u$  is the mean of tidal velocity magnitude (m/s) (Simpson and  
201 Hunter, 1974). Where tidal mixing occurs, it can flux nutrients from depth into the photic zone,  
202 thereby increasing primary productivity. This mixing occurs in the summer months when the  
203 solar radiation is sufficiently strong to induce stratification. Simpson and Hunter (1974) cite a  
204 value of between 1.5 and 2.0 for eq. 5 for where the transition between mixed and stratified water  
205 occurs; the tidal front, which has been confirmed with observations in the Celtic Sea (Simpson,  
206 1976). Fig. 7 shows the shift in the tidal fronts through time. For the period 10 ka to 7 ka  
207 there are widespread mixed areas in the English Channel and Southern North Sea. As sea level  
208 rises and becomes similar to modern day these fronts become very similar to those found today  
209 (Pingree and Griffiths, 1978), apart from those in the Celtic and Irish Seas. Those fronts develop  
210 around 6ka, but are absent at 4 - 1 ka.

### 211 **Sediment grain size changes**

212 Changes in sediment grain size largely follow the changes in tidal range (Fig. 8). Generally  
213 there is a increase in grain size deposited with time, with fine grains dominating 10 ka and areas  
214 becoming dramatically coarser by around 7 ka and then stabilising. The largest changes occur  
215 between 10 ka and 7 ka in the English channel. In the modern there are two main areas of very  
216 coarse sand deposition in the English channel - on in the narrow seaway between England and  
217 France and a large area between the south cost of England and Brittany. These a re largely  
218 stable until around 7 ka when the northern patch shrinks whilst the southern area grows. As the  
219 English Channel shrinks this southern patch of coarse sediment shifts southwards and eventually  
220 decreases in area by 10 ka. These results are similar to the tidal bed shear stress calculated by  
221 Neill et al. (2010) and Ward et al. (2016), though as with the tidal characteristics there are minor  
222 differences in places.

## 223 **DISCUSSION**

224 In order to calculate sea level since the Last Glacial Maximum we must first find data that  
225 indicate past sea level. These data points are located within a tidal range, however; so in order  
226 to place past mean sea level an estimate of past tidal range is required (Shennan, 2015). It is  
227 important to understand past sea level changes as they relate directly to our estimates of the  
228 amount of water sequester by ice sheets during the Last Glacial maximum Clark and Tarasov  
229 (2014) and what drives local, regional and global sea level chnage through time (Shennan et al.,  
230 2018). Here, I present calculations of past tides of the NW European continental shelf using a  
231 finite element model on a multi-scale unstructured mesh. The output of these model simulations  
232 are available for other researchers to use.

233 The tidal characteristics of the European continental shelf show major changes over the past  
234 10,000 years. Most of those changes are associated with the flooding in the southern North Sea

235 from 10 ka to 7 ka. From 7 ka to the present day most tidal properties show little variation. The  
236 exception to this is at 4 ka. At this time the amphidromic point for the  $M_2$  tide shifts westwards  
237 in the southern North Sea moving the corresponding  $M_2$  low amplitude with it. This in turn  
238 alters tidal range and bed shear stresses in the region. By 3 ka the amphidromic point shifts  
239 eastward again, closer to the modern day location.

240 The shifts in tidal characteristic also have implications in the primary productivity potential  
241 of the European shelf. From 10 ka to 7 ka there was a much larger mixed region in the English  
242 Channel with associated tidal fronts. These are associated with both shallower water and higher  
243 tidal velocities. These fronts would have increased the primary productivity in the region as tidal  
244 fronts are a significant percentage of primary productivity in the modern North Sea (Heath and  
245 Beare, 2008). This in turn has implications for changes in the biogeochemistry of the North  
246 Sea since the Last Glacial Maximum. The present day North Sea is thought to store around 250  
247 MT of Particulate Organic Matter (POC) in the top 10 cm of sediment (Diesing et al., 2017).  
248 Given that the North Atlantic biological pump increased the draw down of carbon during the  
249 Last Glacial Maximum (Yu et al., 2019), the increased number of tidal fronts may have had an  
250 impact on the POC stored in North Sea sediments.

251 The model results presented here have a number of limitations. Firstly, the boundary  
252 forcing along the continental shelf are derived from modern data with no corrections for global  
253 palaeobathymetric changes. This is in contrast to both Neill et al. (2010) and Ward et al. (2016).  
254 As the ice sheets in the northern hemisphere grew, they caused changes in the global tidal  
255 dynamics. However, the tidal forcing was still strong in this region and broadly comparable to  
256 modern tides at least until 10 ka, based on previous modelling of global tides (Uehara et al.,  
257 2006). Future work will use global tidal models to estimate the tidal boundary forcing on  
258 global palaeobathymetries to enable simulations to be carried out for reconstructions older than  
259 10 ka. Second, the model also lacks inundation of low-lying land due to tidal movement with  
260 bathymetry 'dredged' to a minimum of 6 m water depth. This is a particular problem in estuaries  
261 and where most SLIP data are collected. This is similar to both Neill et al. (2010) and Ward et al.  
262 (2016) as neither used any wetting and drying algorithms. Whilst the modelled tidal range is not  
263 significantly affected the tidal range must instead be taken from a nearby point rather than the  
264 precise location of the SLIP. Future work will correct this by adding inundation and increase the  
265 spatial resolution around the coast.

266 The results presented here form only part of the solution for correcting SLIPs for palaeo-tidal  
267 range. Once a SLIP is corrected for temporal variations in tidal range, the GIA models then  
268 need correcting as they use SLIPs as a constraint, which in turn alters the palaeobathymetry on  
269 which the tidal model is based. This presents something of a circular problem. Neill et al. (2010)  
270 proposed a methodology whereby some SLIPs are held back from a GIA model to provide a  
271 validation-calibration test. However, here, I have used a different palaeobathymetry to Neill et al.  
272 (2010) and modern forcing as opposed to palaeotidal estimates. Similarly, Ward et al. (2016)  
273 used updated GIA models (same as this work) and a higher model resolution than Neill et al.  
274 (2010). Despite these minor differences in boundary forcing, palaeobathymetric reconstructions,  
275 and numerical implementations, our estimates of tidal range changes are very similar. This is  
276 encouraging as it means that tidal range estimates are not overly sensitive to minor variations in  
277 tidal forcing or palaeobathymetric estimates. It should therefore be possible to correct SLIPs  
278 for tidal range, alter the palaeobathymetry and proceed in an iterative fashion until there are no  
279 changes to the tidal estimates – in essence convergence onto our best estimate. Making use of  
280 modern numerical techniques such as adjoint solvers would aid in estimating the sensitivity of the  
281 tidal model to errors in palaeobathymetry. In turn the sensitivity and error across multiple models  
282 and bathymetric estimates could be used in a Bayesian framework similar to that proposed by  
283 (Cahill et al., 2016). It would then be possible to account for uncertainty and sensitivity in the

284 SLIP height (including tidal range corrections and the uncertainties within those) and the dating  
285 method when deriving sea level estimates.

## 286 CONCLUSIONS

287 The results published here form a palaeotidal database made freely available for future researchers.  
288 The outputs of the model shows significant changes to tidal range, tidal sediment distribution  
289 and the tidal components on the NW European shelf area. These data are the first derived on an  
290 unstructured mesh model where the mesh resolution of the model can vary spatially, allowing  
291 focusing of results in areas of interest (here the coastline) whilst minimising computations time.  
292 Unstructured meshes also reproduce bathymetry and coastlines without staircase effects. This is  
293 an advance over previous modelling studies that used relatively coarse rectilinear grids.

## 294 DATA AVAILABILITY

295 Each time slice is available as a NetCDF file which contains tidal amplitudes and phases for  
296 each tidal component, maximum and mean bed shear stress and velocity vectors, along with  
297 a simple R script to extract nearest data from a list of points. These are available via: DOI:  
298 [10.6084/m9.figshare.6993956](https://doi.org/10.6084/m9.figshare.6993956).

## 299 ACKNOWLEDGEMENTS

300 This project was undertaken on the Viking Cluster, which is a high performance compute facility  
301 provided by the University of York. I am grateful for computational support from the University  
302 of York High Performance Computing service, Viking and the Research Computing team. I  
303 would also like to thank Graham Rush and Fiona Hibbert (University of York) for commenting  
304 on drafts of the manuscript.

## 305 REFERENCES

- 306 Austin, R. M. (1991). Modelling Holocene tides on the NW European continental shelf. *Terra*  
307 *Nova*, 3(3):276–288.
- 308 Avdis, A., Candy, A. S., Hill, J., Kramer, S. C., and Piggott, M. D. (2018). Efficient unstructured  
309 mesh generation for marine renewable energy applications. *Renewable Energy*, 116:842–856.
- 310 Balay, S., Abhyankar, S., Adams, M. F., Brown, J., Brune, P., Buschelman, K., Dalcin, L., Dener,  
311 A., Eijkhout, V., Gropp, W. D., Kaushik, D., Knepley, M. G., May, D. A., McInnes, L. C.,  
312 Mills, R. T., Munson, T., Rupp, K., Sanan, P., Smith, B. F., Zampini, S., Zhang, H., and Zhang,  
313 H. (2018). PETSc users manual. Technical Report ANL-95/11 - Revision 3.9, Argonne  
314 National Laboratory.
- 315 Bockelmann, F.-D., Puls, W., Kleeberg, U., Müller, D., and Emeis, K.-C. (2018). Mapping mud  
316 content and median grain-size of North Sea sediments – A geostatistical approach. *Marine*  
317 *geology*, 397:60–71.
- 318 Bradley, S. L., Milne, G. A., Shennan, I., and Edwards, R. (2011). An improved glacial isostatic  
319 adjustment model for the British Isles. *Journal of Quaternary Science*, 26(5):541–552.
- 320 Cahill, N., Kemp, A. C., Horton, B. P., and Parnell, A. C. (2016). A Bayesian hierarchical model  
321 for reconstructing relative sea level: from raw data to rates of change. *Climate of the Past*,  
322 12(2):525–542.
- 323 Clark, P. U. and Tarasov, L. (2014). Closing the sea level budget at the Last Glacial Maxi-  
324 mum. *Proceedings of the National Academy of Sciences of the United States of America*,  
325 111(45):15861–15862.



- 326 Collins, D. S., Avdis, A., Allison, P. A., Johnson, H. D., Hill, J., and Piggott, M. D. (2018).  
327 Controls on tidal sedimentation and preservation: insights from numerical tidal modelling in  
328 the Late Oligocene–Miocene South China Sea, Southeast Asia. *Sedimentology*.
- 329 Collins, D. S., Avdis, A., Allison, P. A., Johnson, H. D., Hill, J., Piggott, M. D., Amir Hassan,  
330 M. H., and Damit, A. R. (2017). Tidal dynamics and mangrove carbon sequestration during  
331 the Oligo–Miocene in the South China Sea. *Nature communications*, 8:ncomms15698.
- 332 Cotter, C. J. and Ham, D. A. (2011). Numerical wave propagation for the triangular P1DG–P2  
333 finite element pair. *Journal of computational physics*, 230(8):2806–2820.
- 334 Cotter, C. J., Ham, D. A., and Pain, C. C. (2009a). A mixed discontinuous/continuous finite  
335 element pair for shallow-water ocean modelling. *Ocean Modelling*, 26:86–90.
- 336 Cotter, C. J., Ham, D. A., Pain, C. C., and Sebastian, R. (2009b). LBB stability of a mixed  
337 Galerkin finite element pair for fluid flow simulations. *Journal of computational physics*,  
338 228(2):336–348.
- 339 Cummins, P. F. and Thupaki, P. (2017). A note on evaluating model tidal currents against  
340 observations. *Continental shelf research*.
- 341 Diesing, M., Kröger, S., Parker, R., Jenkins, C., Mason, C., and Weston, K. (2017). Predicting the  
342 standing stock of organic carbon in surface sediments of the North-West European continental  
343 shelf. *Biogeochemistry*, 135(1):183–200.
- 344 Heath, M. R. and Beare, D. J. (2008). New primary production in northwest European shelf seas,  
345 1960–2003. *Marine ecology progress series*, 363:183–203.
- 346 Hill, D. F. (2016). Spatial and Temporal Variability in Tidal Range: Evidence, Causes, and  
347 Effects. *Current Climate Change Reports*, 2(4):232–241.
- 348 Hinton, A. C. (1992). Palaeotidal changes within the area of the Wash during the Holocene.  
349 *Proceedings of the Geologists' Association. Geologists' Association*, 103:259–272.
- 350 Imperial College London AMCG (2015). Fluidity manual v4.1.12. *figshare*.
- 351 Lambeck, K., Rouby, H., Purcell, A., Sun, Y., and Sambridge, M. (2014). Sea level and global  
352 ice volumes from the Last Glacial Maximum to the Holocene. *Proceedings of the National  
353 Academy of Sciences of the United States of America*, 111(43):15296–15303.
- 354 Lambrechts, J., Comblen, R., Legat, V., Geuzaine, C., and Remacle, J.-F. (2008). Multiscale  
355 mesh generation on the sphere. *Ocean Dynamics*, 58(5-6):461–473.
- 356 Lyard, F., Lefevre, F., Letellier, T., and Francis, O. (2006). Modelling the global ocean tides:  
357 modern insights from FES2004. *Ocean Dynamics*, 56(5):394–415.
- 358 Martin-Short, R., Hill, J., Kramer, S. C., Avdis, A., Allison, P. A., and Piggott, M. D. (2015).  
359 Tidal resource extraction in the Pentland Firth, UK: Potential impacts on flow regime and  
360 sediment transport in the Inner Sound of Stroma. *Renewable Energy*, 76(0):596–607.
- 361 Neill, S. P., Scourse, J. D., and Uehara, K. (2010). Evolution of bed shear stress distribution  
362 over the northwest European shelf seas during the last 12,000 years. *Ocean Dynamics*,  
363 60(5):1139–1156.
- 364 Peraire, J. and Persson, P. (2008). The Compact Discontinuous Galerkin (CDG) Method for  
365 Elliptic Problems. *SIAM Journal of Scientific Computing*, 30(4):1806–1824.
- 366 Piggott, M. D., Gorman, G. J., Pain, C. C., Allison, P. A., Candy, A. S., Martin, B. T., and  
367 Wells, M. R. (2008). A new computational framework for multi-scale ocean modelling based  
368 on adapting unstructured meshes. *International Journal for Numerical Methods in Fluids*,  
369 56(8):1003–1015.
- 370 Pingree, R. D. and Griffiths, D. K. (1978). Tidal fronts on the shelf seas around the British Isles.  
371 *Journal of geophysical research*, 83(C9):4615–4622.
- 372 Shennan, I. (2015). Handbook of sea-level research: framing research questions. In Shennan, I.,  
373 Long, A. J., and Horton, B. P., editors, *Handbook of Sea-Level Research*, volume 113, pages  
374 3–25. John Wiley & Sons, Ltd, Chichester, UK.

- 375 Shennan, I., Bradley, S. L., and Edwards, R. (2018). Relative sea-level changes and crustal  
376 movements in Britain and Ireland since the Last Glacial Maximum. *Quaternary science*  
377 *reviews*, 188:143–159.
- 378 Shennan, I. and Horton, B. (2002). Holocene land-and sea-level changes in Great Britain. *Journal*  
379 *of Quaternary Science: Published for the Quaternary Research Association*, 17(5-6):511–526.
- 380 Simpson, J. H. (1976). A boundary front in the summer regime of the Celtic Sea. *Estuarine and*  
381 *Coastal Marine Science*, 4(1):71–81.
- 382 Simpson, J. H. and Hunter, J. R. (1974). Fronts in the Irish Sea. *Nature*, 250(5465):404–406.
- 383 Uehara, K., Scourse, J. D., Horsburgh, K. J., Lambeck, K., and Purcell, A. P. (2006). Tidal  
384 evolution of the northwest European shelf seas from the Last Glacial Maximum to the present.  
385 *Journal of geophysical research*, 111(C9):235.
- 386 van de Plassche, O., editor (1986). *Sea-Level Research*. Springer Netherlands, Dordrecht.
- 387 Ward, S. L., Neill, S. P., Scourse, J. D., Bradley, S. L., and Uehara, K. (2016). Sensitivity of  
388 palaeotidal models of the northwest European shelf seas to glacial isostatic adjustment since  
389 the Last Glacial Maximum. *Quaternary science reviews*, 151:198–211.
- 390 Ward, S. L., Neill, S. P., Van Landeghem, K. J. J., and Scourse, J. D. (2015). Classifying seabed  
391 sediment type using simulated tidal-induced bed shear stress. *Marine geology*, 367:94–104.
- 392 Weatherall, P., Marks, K. M., Jakobsson, M., Schmitt, T., Tani, S., Arndt, J. E., Rovere, M.,  
393 Chayes, D., Ferrini, V., and Wigley, R. (2015). A new digital bathymetric model of the world's  
394 oceans. *Life support & biosphere science: international journal of earth space*, 2(8):331–345.
- 395 Wells, M. R., Allison, P. A., Hampson, G. J., Piggott, M. D., and Pain, C. C. (2005a). Mod-  
396 elling ancient tides: the Upper Carboniferous epi-continental seaway of Northwest Europe.  
397 *Sedimentology*, 52(4):715–735.
- 398 Wells, M. R., Allison, P. A., Piggott, M. D., Gorman, G. J., Hampson, G. J., Pain, C. C., and Fang,  
399 F. (2007). Numerical Modeling of Tides in the Late Pennsylvanian Midcontinent Seaway of  
400 North America with Implications for Hydrography and Sedimentation. *Journal of Sedimentary*  
401 *Research*, 77(10):843–865.
- 402 Wells, M. R., Allison, P. A., Piggott, M. D., Hampson, G. J., Pain, C. C., and Gorman, G. J.  
403 (2010). Tidal Modeling of an Ancient Tide-Dominated Seaway, Part 1: Model Validation and  
404 Application to Global Early Cretaceous (Aptian) Tides. *Journal of Sedimentary Research*,  
405 80(5):393–410.
- 406 Wells, M. R., Allison, P. A., Piggott, M. D., Pain, C. C., Hampson, G. J., and DE Oliviera, C.  
407 R. E. (2005b). Large sea, small tides: the Late Carboniferous seaway of NW Europe. *Journal*  
408 *of the Geological Society*, 162(3):417–420.
- 409 Wessel, P. and Smith, W. H. F. (1996). A Global Self-consistent, Hierarchical, High-resolution  
410 Shoreline Database. *Journal of geophysical research*, 101(B4):8741–8743.
- 411 Yu, J., Menviel, L., Jin, Z. D., Thornalley, D. J. R., Foster, G. L., Rohling, E. J., McCave,  
412 I. N., McManus, J. F., Dai, Y., Ren, H., He, F., Zhang, F., Chen, P. J., and Roberts, A. P.  
413 (2019). More efficient North Atlantic carbon pump during the Last Glacial Maximum. *Nature*  
414 *communications*, 10(1):2170.

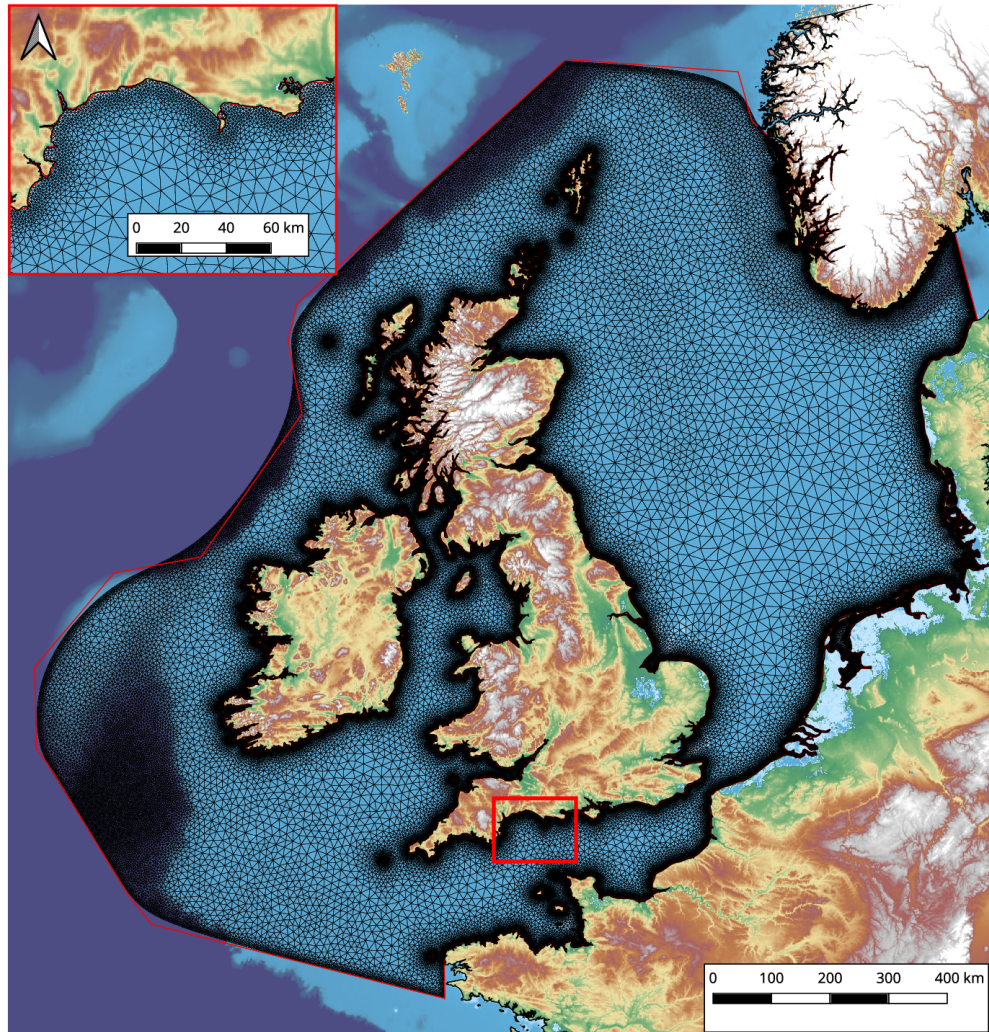


**Figure 2.** Modern multiscale mesh using GSHHS coastlines (high resolution). Mesh resolution is smallest around coastlines and deeper water. Red line shows the coastline from GSHHS, black is the mesh, and colours show height from the GEBCO bathymetry/topography. A close-up of the south coast of England is shown to highlight the mesh resolution change with respect to the coastline.

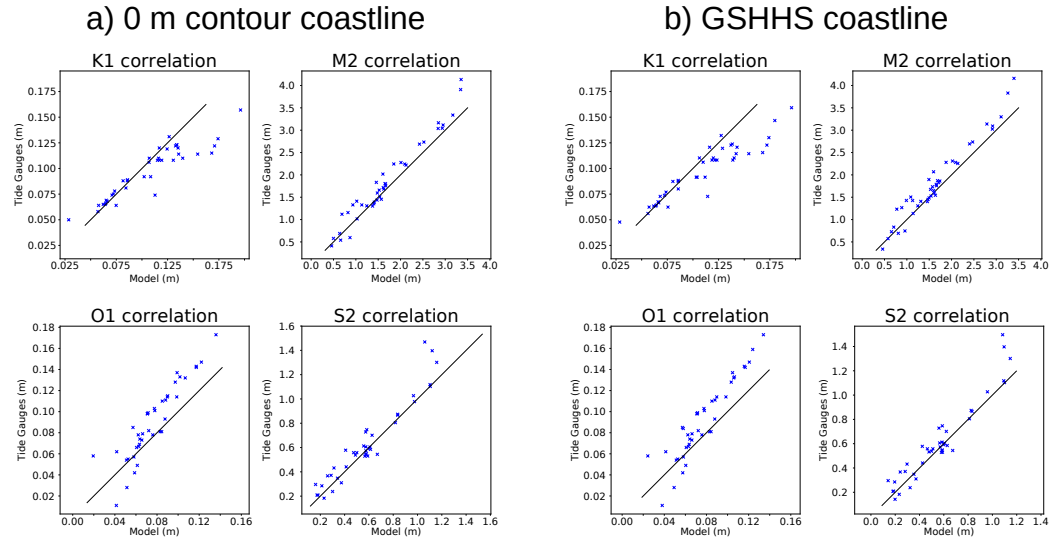


**Figure 3.** Cross plot of amplitudes generated from Fluidty against tide gauges for four main tidal components using either the 0 m contour (a) or high resolution GSHHS data (b) as the coastline.

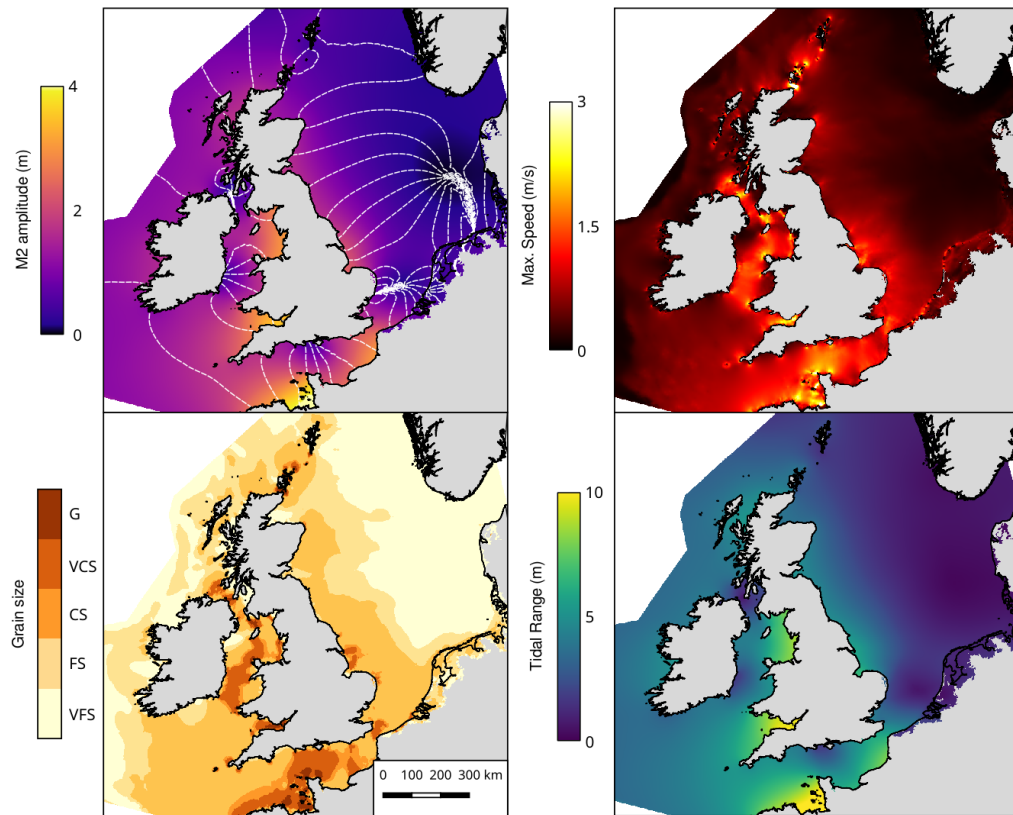


**Figure 4.** Tidal properties of the present day. Top left: M<sub>2</sub> amplitude and phase. Top right: maximum speed over the 30 day simulation. Bottom left: grain size derived from maximum bed shear stress. Bottom right: tidal range.

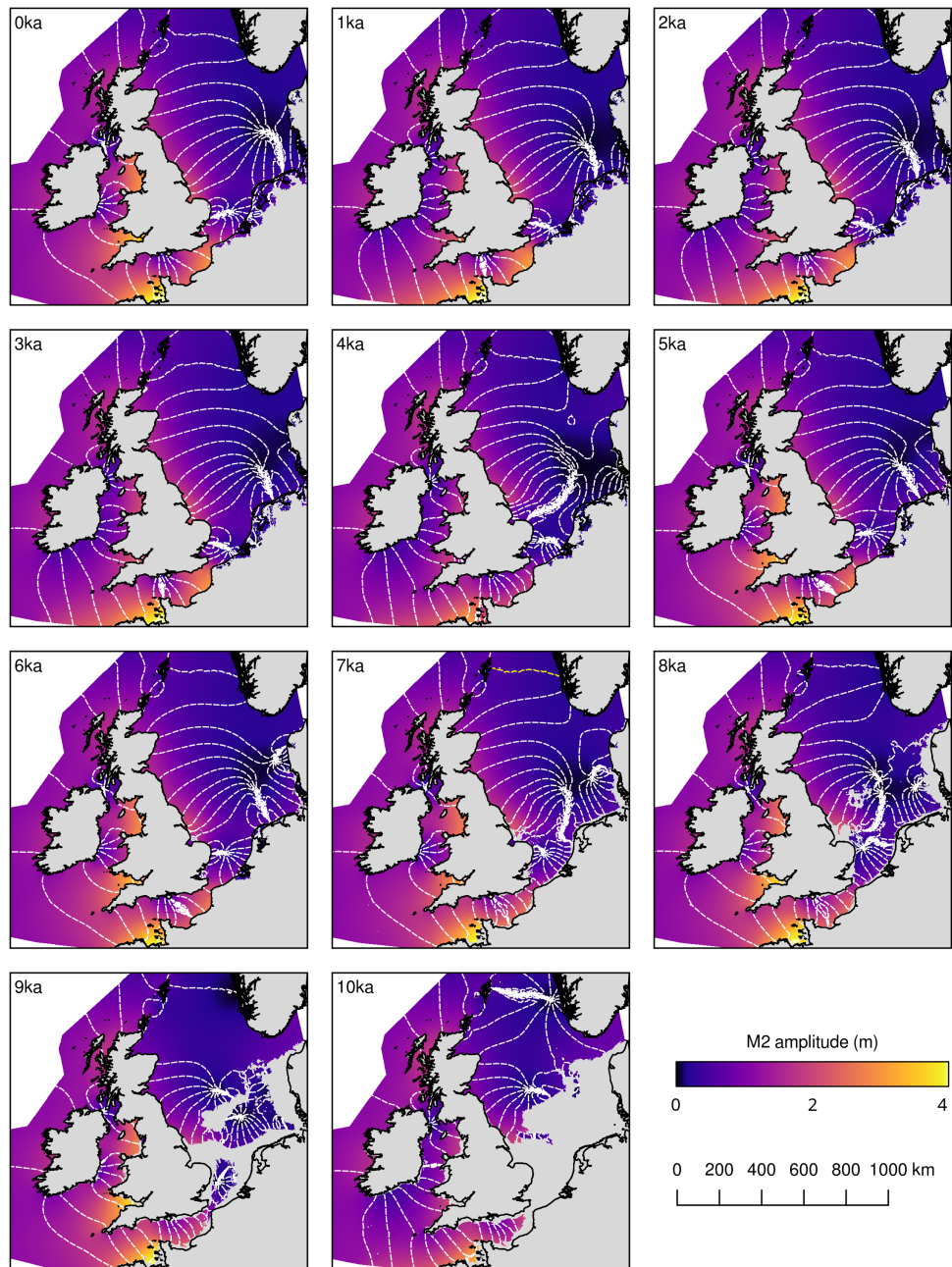


**Figure 5.**  $M_2$  amplitude (colour bar) and phase (contour lines) for each of the time slices from present day to 10 ka. Grey shading indicates land and the modern coastline is shown in a thick black line.

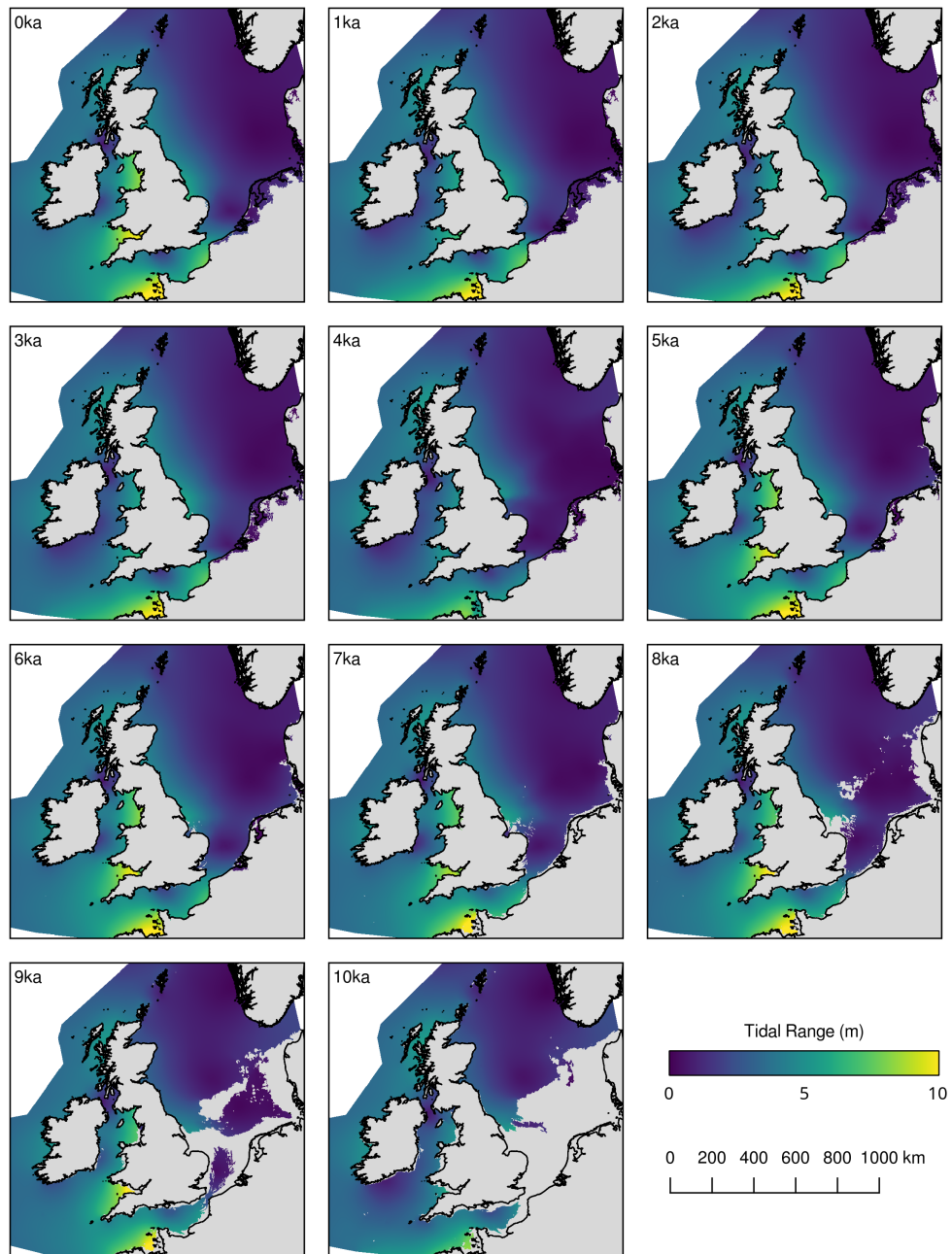


**Figure 6.** Tidal range in the NW European shelf for each timeslice from present day to 10 ka. Add palaeo shorelines. Grey shading indicates land and the modern coastline is shown in a thick black line.

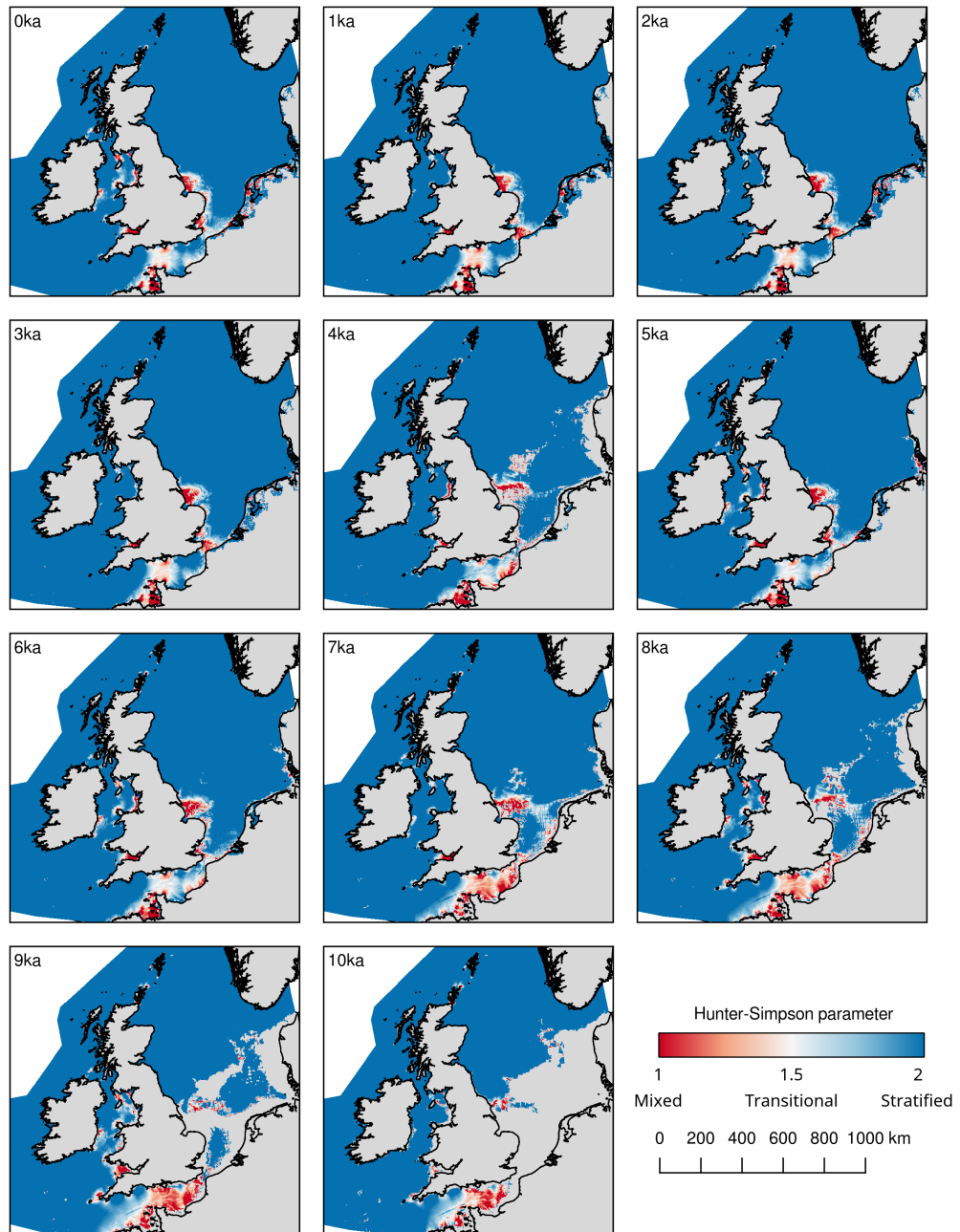


**Figure 7.** Estimates of the Hunter-Simpson parameter over the last 10,000 years. Blue colours show summer stratification and red show mixed regions. The transition through white colours shows the location of tidal mixing fronts. Grey shading indicates land and the modern coastline is shown in a thick black line.

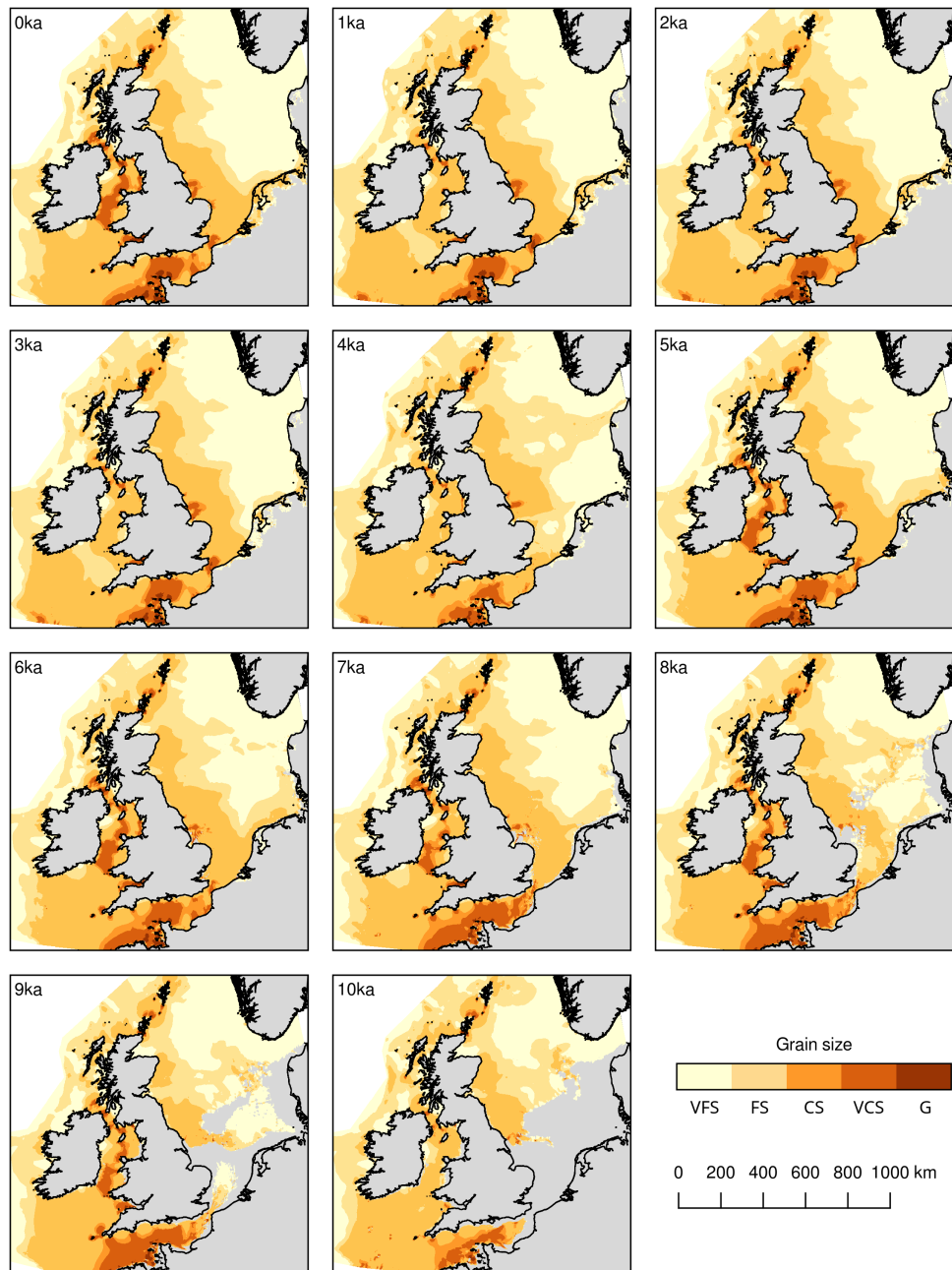


**Figure 8.** Sediment grain size derived from maximum bed shear stress predicted from the tidal model corrected using the method detailed in [Ward et al. \(2015\)](#). Grey shading indicates land and the modern coastline is shown in a thick black line.